

A tensor network representation of path integrals: Implementation and analysis

Amartya Bose*

Department of Chemistry, Princeton University, Princeton, New Jersey 08544

Peter L. Walters*

Tensors with finite correlation afford very compact tensor network representations. A novel tensor network-based decomposition of real-time path integral simulations involving Feynman-Vernon influence functional is introduced. In this tensor network path integral (TNPI) technique, the finite temporarily non-local interactions introduced by the influence functional can be captured very efficiently using matrix product state representation for the path-dependent Green’s function (PDGF). We illustrate this particular TNPI method through various illustrative examples, including a charge transfer and exciton transfer in a dimer, and show how it is readily applied to systems with greater than two states. PDGF-TNPI utilizes the symmetries of the problem, leading to accelerated convergence and dramatic reductions of computational effort. We also introduce an approximate method that speeds up propagation beyond the non-local memory length. Furthermore, the structure imposed by the tensor network representation of the PDGF naturally suggests other factorizations that make simulations for extended systems more efficient. These factorizations would be the subject of future explorations. The flexibility of the PDGF-TNPI framework makes it a promising new addition to the family of path integral methods for non-equilibrium quantum dynamics.

I. INTRODUCTION

Quantum mechanics plays an important role in various condensed phase dynamical processes. While there are certain processes, such as calculation of vibrational spectra, that can be simulated using classical mechanics [1], dynamical problems that involve deep tunneling through potential barriers like charge or excitonic transfer are essentially quantum mechanical in nature. Simulation of these quantum processes in condensed phase environments is an extremely challenging task owing to the exponential growth of computational complexity with the degrees of freedom of the system being studied. Wave function based methods like multi-configuration time-dependent Hartree (MCTDH) [2, 3] and time-dependent density matrix renormalization group (tDMRG) [4–6], for example, are extremely powerful in efficiently simulating the dynamics of certain classes of systems; however, they are not appropriate for working with arbitrary condensed phase problems, where a manifold of energy levels is thermally accessible.

Over the years, there has been an explosion of methods that attempt to solve the problem of thermal quantum dynamics in a condensed phase. Most of these methods can be categorized into two groups: approximate methods or quantum-classical methods. Approximate methods tend to treat the entire system under study using “augmented” classical trajectories. The most prominent methods of this group are the various approaches based on the semiclassical approximation [7–11], centroid molecular dynamics [12, 13] and ring polymer molecular dynamics [14–16] for Born-Oppenheimer dynamics, and the family of surface hopping methods [20–23] for non-

adiabatic processes. The quantum-classical methods, on the other hand, typically identify a reduced-dimensional quantum “system” and relegate the rest of the degrees of freedom to a classical treatment, thereby effectively restricting the exponential growth of complexity of quantum dynamics to only the system degrees of freedom. Various rigorous quantum-classical approaches have been developed over the years such as quantum-classical Liouville dynamics [24] and quantum-classical path integral (QCPI) [25–28]. Because the system is now treated using exact quantum mechanics all effects stemming from non-adiabaticity are rigorously accounted for.

Amongst the class of problems that can be solved using the system-solvent decomposition, if the solvent can be modelled as a bath of harmonic oscillators, the reduced density matrix of the system can be rigorously simulated without classical trajectories using the Feynman-Vernon influence functionals (IF) [29]. Though general condensed phase solvents are anharmonic, over the years, the harmonic bath mapping, obtained via linear response theory, has repeatedly been shown to give impressively accurate results for a variety of systems [30]. The quasi-adiabatic propagator path integral (QuAPI) [31, 32] and methods based on QuAPI [33–36] enable efficient simulations of the dynamics of systems coupled bi-linearly to harmonic baths.

The biggest challenge of evaluating the real-time path integral is the non-local nature of the IF. This non-Markovian memory leads to an exponential growth of the number of paths that need to be tracked. However, the memory has a finite length, which means that the entanglement between time points along a path has a finite range. Tensors with finite entanglement can on many occasions be very compactly represented using tensor networks. For instance, with extended quantum systems, the dimensionality of the Hilbert space grows exponentially with the number of particles. How-

* Both authors contributed equally to this work.

ever, matrix-product states (MPSs) and other tensor network decompositions allow efficient representations of many such systems. This is why TN structures are used in DMRG [5, 37–41] and other methods optimized for simulating multiple dimensions and critical phenomena like the projected entangled-pair state (PEPS) [42] and the multiscale entanglement renormalization ansatz (MERA) [43, 44] to efficiently represent the wave function. In this paper, we introduce a tensor-network method to perform path integral simulations for systems coupled with a dissipative medium. This method, the path-dependent Green’s function-based tensor network path integral (PDGF-TNPI), uses MPSs to compress the representation of paths involved in path integral simulations. Consequently, the influence functional becomes a matrix-product operator (MPO) that acts on the PDGF MPS. Much work has been done in finding efficient methods of applying an MPO to an MPS. Not only can the PDGF-TNPI method automatically take advantage of these advances, but through a careful construction of the influence functional MPO, we exploit certain symmetries present in the problem. In this work, we utilize the open source ITensor library [45] as the basis of our PDGF-TNPI implementation, as it provides for an efficient means of evaluating the relevant tensor operations.

In Sec. II, we discuss the PDGF-TNPI method, detailing a construction that results in a simple, elegant and efficient structure. We also demonstrate an approximation that emerges naturally from the resulting structure. This “Markovian iteration scheme” approximation which is able to speed up simulations involving processes with very long time-scales and comparatively short memory lengths. Thereafter, in Sec. III, we illustrate the use of the method through numerous examples. Apart from a direct comparison with QuAPI, we apply PDGF-TNPI to study charge and exciton transfer dynamics. We demonstrate the ability of PDGF-TNPI to develop an optimized representation enabling us to access extremely long memory times even with very modest computational resources. Finally, we end the paper in Sec. IV with some concluding remarks, and outlook for further developments based on, and facilitated by PDGF-TNPI.

II. METHODOLOGY

Consider a potentially time-dependent quantum system interacting bi-linearly with a harmonic bath. The Hamiltonian is given as:

$$\hat{H} = \hat{H}_0(t) + \hat{H}_b(\hat{x}_j, \hat{p}_j, \hat{s}) \quad (1)$$

$$\hat{H}_b(\hat{x}_j, \hat{p}_j, \hat{s}) = \sum_j \frac{\hat{p}_j^2}{2m_j} + \frac{1}{2} m_j \omega_j^2 \left(\hat{x}_j - \frac{c_j \hat{s}}{m_j \omega_j^2} \right)^2 \quad (2)$$

where $\hat{H}_0(t)$ is the Hamiltonian of the isolated D -state quantum system, and \hat{H}_b is the Hamiltonian for the bath and the system-bath interactions. These interactions are

defined in terms of ω_j and c_j , which are the frequency and the coupling strength of the j^{th} bath mode, respectively. The system position operator is \hat{s} . The system-bath interaction is characterized by the spectral density [46]:

$$J(\omega) = \frac{\pi}{2} \sum_j \frac{c_j^2}{m_j \omega_j} \delta(\omega - \omega_j). \quad (3)$$

The spectral density is related to the energy gap autocorrelation function via a Fourier transform [30]. For most classical solvents, this autocorrelation function is computed using classical trajectories on an appropriately parameterized force field.

The dynamics of the isolated D -state system can be obtained by directly solving the time-dependent Schrödinger equation for the propagator:

$$i\hbar \frac{\partial \hat{U}_0(t_0, t)}{\partial t} = \hat{H}_0(t) \hat{U}_0(t_0, t), \quad (4)$$

where $\hat{U}_0(t_0, t)$ is the propagator evolving the system from an initial state at time t_0 to a final state at time t . The density matrix is propagated using a combination of forward and backward propagators; this combined forward-backward propagator, K_j , connecting states at time point $t_0 = (j-1)\Delta t$ to $t = j\Delta t$ is given by:

$$K_j(s_{j-1}^{\pm}, s_j^{\pm}, \Delta t) = \langle s_j^+ | \hat{U}_0((j-1)\Delta t, j\Delta t) | s_{j-1}^+ \rangle \\ \times \langle s_{j-1}^- | \hat{U}_0^\dagger((j-1)\Delta t, j\Delta t) | s_j^- \rangle. \quad (5)$$

Suppose that the system and bath are initially uncoupled and that the bath is in a thermal equilibrium $\rho_b(\beta)$ at an inverse temperature of β . The reduced density matrix at a final time, $\langle s_N^+ | \tilde{\rho}(N\Delta t) | s_N^- \rangle = \tilde{\rho}(s_N^{\pm}, N\Delta t)$, can be obtained using a discretized path integral representation as follows:

$$\tilde{\rho}(s_N^{\pm}, N\Delta t) = \text{Tr}_b \langle s_N^+ | \hat{U}(t) \tilde{\rho}(0) \otimes \rho_b(\beta) \hat{U}^\dagger(t) | s_N^- \rangle \\ = \sum_{s_0^{\pm}} \tilde{\rho}(s_0^{\pm}, 0) G(s_0^{\pm}, s_N^{\pm}, N\Delta t) \quad (6)$$

$$G(s_0^{\pm}, s_N^{\pm}, N\Delta t) = \sum_{s_1^{\pm}} \cdots \sum_{s_{N-1}^{\pm}} K_1(s_0^{\pm}, s_1^{\pm}, \Delta t) K_2(s_1^{\pm}, s_2^{\pm}, \Delta t) \\ \cdots K_N(s_{N-1}^{\pm}, s_N^{\pm}, \Delta t) F[\{s_j^{\pm}\}] \quad (7)$$

where Δt is the quantum time-step that was used to discretize the path integral, s_j^{\pm} is the forward-backward state of the system at the j^{th} time point, $G(s_0^{\pm}, s_k^{\pm}, k\Delta t)$ is the Green’s function connecting state s_0 to s_k in k time steps and \hat{U} is the full system-bath propagator. The Feynman-Vernon influence functional [29], $F[\{s_j^{\pm}\}]$, encodes the interaction of the system with the bath and is given as

$$F[\{s_j^{\pm}\}] = \exp \left(-\frac{1}{\hbar} \sum_{0 \leq k \leq N} \Delta s_k \sum_{0 \leq k' \leq k} (\text{Re}(\eta_{kk'})) \Delta s_{k'} \right)$$

$$+2i \operatorname{Im}(\eta_{kk'}) \bar{s}_{k'}) \Big) \quad (8)$$

where $\eta_{kk'}$ are the discretized η -coefficients [31, 32], $\Delta s_k = s_k^+ - s_k^-$ and $\bar{s}_k = \frac{1}{2}(s_k^+ + s_k^-)$.

Generally, QuAPI directly calculates the reduced density matrix using Eq. (6), however there are advantages to calculating the Green's function using Eq. (7). Apart from being independent of the initial state of the system, the Green's function is also important for evaluation of the memory kernel associated with the Nakajima-Zwanzig [47, 48] generalized quantum master equation (GQME). Recently there has been a lot of interest in using approximate [49–52] and numerically exact kernels for solving GQME [53]. Therefore, we formulate TNPI in terms of solving for the Green's function.

First, we define a couple terms that we use to rephrase the problem and build the TNPI algorithm. Consider the bare and full variants of the “path-dependent Green's function” (PDGF) defined respectively as:

$$P_{s_0^\pm \dots s_N^\pm}^{(0)} = K_1(s_0^\pm, s_1^\pm, \Delta t) K_2(s_1^\pm, s_2^\pm, \Delta t) \dots K_N(s_{N-1}^\pm, s_N^\pm, \Delta t) \quad (9)$$

$$P_{s_0^\pm \dots s_N^\pm} = F[\{s_j^\pm\}] P_{s_0^\pm \dots s_N^\pm}^{(0)} \quad (10)$$

The quantities $P^{(0)}$ and P are tensors of rank N with $O(D^{2N})$ coefficients. The Green's function is obtained from the full PDGF tensor by contracting over all but the terminal indices.

$$G(s_0^\pm, s_N^\pm, N\Delta t) = \sum_{s_1^\pm} \dots \sum_{s_{N-1}^\pm} P_{s_0^\pm \dots s_N^\pm} \quad (11)$$

The PDGF would play a fundamental role in the development of the method. Since the number of values required to describe the PDGF grows exponentially with the number of time steps, a direct evaluation or the Green's function is only possible if the number of time steps is small. The goal of using tensor networks is to “factorize” these large tensors into products of many smaller ones; and thus, reduce the cost of evaluation and storage. The optimum structure of the tensor network involved is guided strongly by the exact nature of the tensor under consideration.

It is well known that the non-Markovian memory length of a quantum system interacting with a condensed phase is not infinitely long. Though the non-Markovian interactions do not have a finite support, they decay asymptotically. The relative short-ranged nature of the interaction between time-points imply that the PDGF should be well described as a sequence of tensor products, where each tensor in the sequence corresponds to a different time-point. The resulting factorization gives

$$P_{s_0^\pm \dots s_N^\pm} = \sum_{\{\alpha_j\}} M_{\alpha_0}^{s_0^\pm} M_{\alpha_0, \alpha_1}^{s_1^\pm} \dots M_{\alpha_{N-2}, \alpha_{N-1}}^{s_{N-1}^\pm} M_{\alpha_{N-1}}^{s_N^\pm} \quad (12)$$

which is the MPS representation of the PDGF. In this representation, each tensor in the product is considered to be on a different site. The indices that are used in the superscript are the so-called “site indices” and they correspond to the forward-backward state of the system at the different time points. The indices in the subscript are the so-called “bond indices,” the dimensions of which are closely related to the length of the non-Markovian memory. In principle this factorization is exact; however, for an arbitrary PDGF, the size of the largest bond index (i.e., the maximum “bond dimension”) is $O(D^N)$. In practice, the bond dimensions are truncated and treated as convergence parameters. We will show in Sec. III, that the actual bond dimensions needed in a simulation are quite small.

The presence of the influence functional in the description of the full PDGF (Eq. (10)) prevents us from forming simple expressions for the tensors in Eq. (12); however, as we will now show, this is not the case for the bare PDGF. Consider the singular value decomposition (SVD) of the forward-backward propagator:

$$K_j(s_{j-1}^\pm, s_j^\pm, \Delta t) = \sum_{\alpha_{j-1}} U_{\alpha_{j-1}}^{s_{j-1}^\pm} \times R_{\alpha_{j-1}}^{s_j^\pm} \quad (13)$$

$$R_{\alpha_{j-1}}^{s_j^\pm} = \sum_{\beta} S_{\alpha_{j-1}, \beta} \times V_{\beta}^{s_j^\pm \dagger} \quad (14)$$

where S is the diagonal matrix of the nonzero singular values, U and V are the matrices of the left and right singular vectors respectively. Substituting this into Eq. (9), we get the required expressions for the tensors appearing in Eq. (12). Thus, for a bare PDGF:

$$M_{\alpha_0}^{s_0^\pm} = U_{\alpha_0}^{s_0^\pm}, \quad (15)$$

$$M_{\alpha_{N-1}}^{s_{N-1}^\pm} = R_{\alpha_{N-1}}^{s_{N-1}^\pm}, \quad (16)$$

$$M_{\alpha_{j-1}, \alpha_j}^{s_{j-1}^\pm, s_j^\pm} = R_{\alpha_{j-1}}^{s_{j-1}^\pm} U_{\alpha_j}^{s_j^\pm} \quad 0 < j < N. \quad (17)$$

It is worth noting that, in this case, the factorization is exact, and the bond dimensions are independent of the number of time-steps, N . This is a direct consequence of the Markovian nature of the bare PDGF. We schematically depict the bare PDGF as an MPS with red circular nodes as in Fig. 1.

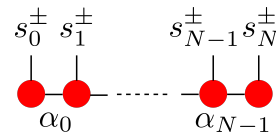


FIG. 1. Schematic diagram for bare PDGF MPS. Red nodes denote the matrices corresponding to the bare system propagator's SVD.

Now that we have described how to deal with the bare system, let us consider the influence functional. From Eq. (10), we see that to obtain the full PDGF, the influence functional must be applied to the bare PDGF. In

the TN framework, a MPO acts on a MPS to produce another MPS; therefore, we want to construct an influence functional MPO, which, when applied to the bare PDGF MPS, gives the PDGF MPS for the full system-bath problem. The influence functional can be rewritten as a product of influence functionals coming from the interactions with different end-points

$$F[\{s_j^\pm\}] = \prod_{0 \leq k \leq N} F_k[\{s_j^\pm\}] \quad (18)$$

$$F_k[\{s_j^\pm\}] = \exp \left(-\frac{1}{\hbar} \Delta s_k \sum_{0 \leq k' \leq k} (\text{Re}(\eta_{kk'}) \Delta s_{k'} + 2i \text{Im}(\eta_{kk'}) \bar{s}_{k'}) \right). \quad (19)$$

The influence functional corresponding to a particular last time point, $F_k[\{s_j^\pm\}]$ given by Eq. (19), can be expressed as an MPO. We will construct this MPO in two steps by grouping the forward-backward states by the unique values of Δs . First, consider the trivial case when $\Delta s_k = 0$, and note that for all these states, $F_k = 1$, or as an operator, $F_k = \mathbb{I}_0^{\pm} \otimes \mathbb{I}_1^{\pm} \dots \mathbb{I}_{k-1}^{\pm} \otimes \mathcal{P}_0^{s_k^\pm}$ where \mathbb{I}_j^{\pm} is the identity operator in the space of $\{s_j^\pm\}$, and $\mathcal{P}_0^{s_k^\pm}$ is the projection operator on to the space where $\Delta s_k = 0$.

Next, we consider a non-zero value of Δs_k . For all these states, the operators on sites, $k' < k$, are given as $e^{-\frac{1}{\hbar} \Delta s_k (\text{Re}(\eta_{kk'}) \mathbb{D}_{k'} + 2i \text{Im}(\eta_{kk'}) \mathbb{S}_{k'})}$, and the operator on site $k' = k$ as $\mathcal{P}_{\Delta s_k}^{s_k^\pm} e^{-\frac{1}{\hbar} \Delta s_k (\text{Re}(\eta_{kk}) \mathbb{D}_k + 2i \text{Im}(\eta_{kk}) \mathbb{S}_k)}$. Here \mathbb{D}_k and \mathbb{S}_k are the matrices that return the difference and average position of the system corresponding to the forward-backward state. Both the \mathbb{D} and \mathbb{S} operators are diagonal in the s^\pm basis. In this case, the resulting F_k , becomes direct product of these single site operators. We see that F_k is a sum of direct product of operators, where each term in the sum corresponds to a different value of Δs_k . Hence, we can define F_k as a MPO, \mathbb{F}_k , as follows:

$$\mathbb{F}_k = \sum_{\{\beta_j\}} W_{\beta_0}^{s_0^\pm, s_0'^\pm}(\eta_{k0}) \dots W_{\beta_{k'-1}, \beta_{k'}}^{s_{k'}^\pm, s_{k'}'^\pm}(\eta_{kk'}) \times W_{\beta_{k'}, \beta_{k'+1}}^{s_{k'+1}^\pm, s_{k'+1}'^\pm}(\eta_{k(k'+1)}) \dots W_{\beta_{k-1}}^{s_k^\pm, s_k'^\pm}(\eta_{kk}) \quad (20)$$

where $\{\beta_j\}$ are the bond indices. In this case, all the bond dimensions of this MPO are equal to the number of unique values of Δs . We define $f(\beta)$ as the function that when given a value of the bond index β , returns the corresponding value of Δs . Furthermore, we define $\mathcal{P}_{f(\beta)}^{s_k^\pm}$ to be the projection operator on to the space where $\Delta s_k = f(\beta)$. With this notation, now, we can define the various tensors in our influence functional MPO.

$$W_{\beta_0}^{s_0^\pm, s_0'^\pm}(\eta_{k0}) = \delta_{s_0^\pm, s_0'^\pm} \exp \left(-\frac{1}{\hbar} f(\beta_0) (\text{Re}(\eta_{k0}) \Delta s_0 + 2i \text{Im}(\eta_{k0}) \bar{s}_0) \right) \quad (21)$$

$$W_{\beta_{k'-1}, \beta_{k'}}^{s_{k'}^\pm, s_{k'}'^\pm}(\eta_{kk'}) = \delta_{s_{k'}^\pm, s_{k'}'^\pm} \delta_{\beta_{k'-1}, \beta_{k'}} \exp \left(-\frac{1}{\hbar} f(\beta_{k'-1}) (\text{Re}(\eta_{kk'}) \Delta s_{k'} + 2i \text{Im}(\eta_{kk'}) \bar{s}_{k'}) \right) \quad (22)$$

$$W_{\beta_{k-1}}^{s_k^\pm, s_k'^\pm}(\eta_{kk}) = \delta_{s_k^\pm, s_k'^\pm} \mathcal{P}_{f(\beta_{k-1})}^{s_k^\pm} \exp \left(-\frac{1}{\hbar} \Delta s_k (\text{Re}(\eta_{kk}) \Delta s_k + 2i \text{Im}(\eta_{kk}) \bar{s}_k) \right) \quad (23)$$

The MPS representation of the full PDGF can be obtained by iteratively applying the \mathbb{F}_k MPOs to the bare PDGF.

$$P_{s_0^\pm, s_1^\pm}^{(1)} = \sum_{\{\alpha_j'\}} \mathbb{F}_1 P_{s_0^\pm, s_1^\pm}^{(0)} \quad (24)$$

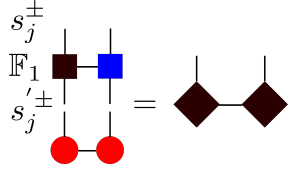
$$P_{s_0^\pm \dots s_k^\pm}^{(k)} = \sum_{\{\alpha_j'\}} \mathbb{F}_k \left(P_{s_0^\pm \dots s_{k-1}^\pm}^{(k-1)} K_{\alpha_{k-1}}^{s_{k-1}^\pm, s_k^\pm} \right) \quad (25)$$

$$P_{s_0^\pm \dots s_N^\pm} = \sum_{\{\alpha_j'\}} \mathbb{F}_N \left(P_{s_0^\pm \dots s_{N-1}^\pm}^{(N-1)} K_{\alpha_{N-1}}^{s_{N-1}^\pm, s_N^\pm} \right) \quad (26)$$

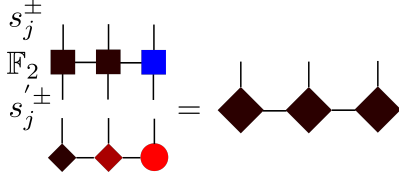
where $\{\alpha_j'\}$ are the new bonds indices produced by the application of the MPO to the MPS. In the above expressions, $P_{s_0^\pm \dots s_k^\pm}^{(k)}$ represents the PDGF MPS after the

k^{th} step of the propagation, and the tensor $K_{\alpha_{k-1}}^{s_{k-1}^\pm, s_k^\pm} = U_{\alpha_{k-1}}^{s_{k-1}^\pm} R_{\alpha_{k-1}}^{s_k^\pm}$ and is associated with the SVD decomposition of the k^{th} forward-backward system propagator, $K_k(s_{k-1}^\pm, s_k^\pm, \Delta t)$ (see Eqs. (5), (9), (13) and (14)). The first couple of steps of the application of the IF MPO are schematically portrayed in Fig. 2.

As we discussed earlier, the non-Markovian memory in a condensed phase process decays to zero, thus we can construct an accurate MPS representation of the PDGF using fairly small values for the bond dimensions. However, the bond dimensions can be further reduced by explicitly truncating the memory. To that end, we define $L\Delta t$ to be the maximum distance, in time, between which the influence functional can couple two forward-backward system points. We see from Eq. (7) that any system points that exceed this difference can be summed independently of each other. This leads us to define the



(a) Calculation of $P^{(1)}$ cf. Eq. (24). Red circles: SVD of forward-backward propagator K . MPS with black diamonds is the full PDGF for two steps.



(b) Calculation of $P^{(2)}$ cf. Eq. (25) starting from $P^{(1)}$ obtained in Fig. 2 (a). Combination of dark red diamond and red circle comes from product of $P^{(1)}$ and K . MPS with black diamonds represents the full PDGF for three steps.

FIG. 2. Schematic diagrams for application of IF MPO.

partially contracted PDGF, as well as the partially contracted IF MPO:

$$\tilde{P}_{s_0^\pm, s_{N-L}^\pm \dots s_N^\pm} = \sum_{s_1^\pm} \dots \sum_{s_{N-L-1}^\pm} P_{s_0^\pm \dots s_N^\pm}, \quad L < N \quad (27)$$

$$\begin{aligned} \tilde{\mathbb{F}}_k &= \sum_{\{\beta_j\}} W_{\beta_0}^{s_0^\pm, s_0^{\prime\pm}}(0) W_{\beta_0, \beta_{k-L}}^{s_{k-L}^\pm, s_{k-L}^{\prime\pm}}(\eta_{k(k-L)}) \\ &\dots W_{\beta_{k-1}, \beta_{k'}}^{s_{k'}^\pm, s_{k'}^{\prime\pm}}(\eta_{kk'}) \dots W_{\beta_{k-1}}^{s_k^\pm, s_k^{\prime\pm}}(\eta_{kk}), \quad L < k \quad (28) \end{aligned}$$

where the W tensors are the same as those defined earlier (see Eqs. (21), (22) and (23)). We can now redefine the iterative procedure described above for calculating the full PDGF MPS, in a manner consistent with an explicit truncation of the memory. When $k \leq L$, the procedure follows Eqs. (24) and (25) exactly. This is called the “full memory” regime. When $k > L$, which is often referred to as the “iteration” regime, we have

$$\tilde{P}_{s_0^\pm \dots s_{L+1}^\pm}^{(L+1)} = \sum_{\{\alpha'_j\}} \tilde{\mathbb{F}}_{L+1} P_{s_0^{\prime\pm} \dots s_L^{\prime\pm}}^{(L)} K_{\alpha_L}^{s_L^{\prime\pm}, s_{L+1}^{\prime\pm}} \quad (29)$$

$$\begin{aligned} \tilde{P}_{s_0^\pm, s_{k-L}^\pm \dots s_k^\pm}^{(k)} &= \sum_{\{\alpha'_j\}} \tilde{\mathbb{F}}_k \left(\sum_{s_{k-L-1}^{\prime\pm}} \tilde{P}_{s_0^{\prime\pm}, s_{k-L-1}^{\prime\pm} \dots s_{k-1}^{\prime\pm}}^{(k-1)} \right. \\ &\quad \left. \times K_{\alpha_{k-1}}^{s_{k-1}^{\prime\pm}, s_k^{\prime\pm}} \right) \quad (30) \end{aligned}$$

$$\tilde{P}_{s_0^\pm, s_{N-L}^\pm \dots s_N^\pm}^{(N)} = \sum_{\{\alpha'_j\}} \tilde{\mathbb{F}}_N \left(\sum_{s_{N-L-1}^{\prime\pm}} \tilde{P}_{s_0^{\prime\pm}, s_{N-L-1}^{\prime\pm} \dots s_{N-1}^{\prime\pm}}^{(N-1)} \right)$$

$$\times K_{\alpha_{N-1}}^{s_{N-1}^{\prime\pm}, s_N^{\prime\pm}} \quad (31)$$

Due to the aforementioned memory truncation, the number of system sites never exceeds $L + 2$. Lastly, the expression for the Green’s function in terms of the partially contracted PDGF is given by

$$G(s_0^\pm, s_N^\pm, N\Delta t) = \sum_{s_{N-L}^\pm} \dots \sum_{s_{N-1}^\pm} \tilde{P}_{s_0^\pm, s_{N-L}^\pm \dots s_N^\pm} \quad (32)$$

As it turns out, this iterative procedure is practically identical to the one used by QuAPI. The key difference is that QuAPI sums over s_0^\pm as soon as $k > L$, but here, its retained as part of the Green’s function.

There are various algorithms for applying an MPO to an MPS. Probably the two most common methods are the direct application followed by an SVD-based compression of the MPS and a variational application of the MPO to the MPS. Paeckel *et al.* [54] have provided a detailed overview of these methods, the computational effort involved and the common pitfalls. Though it is well-known that the variational method can, depending on the initial “guess” MPS, get stuck in metastable states, in our current explorations we have faced no such issues. This might be because for a given time-step, the individual \mathbb{F}_k and $\tilde{\mathbb{F}}_k$ do not significantly alter the MPSs. However, we still checked all the calculations reported against the direct SVD method as well.

In addition to the iterative algorithms we have outlined till now, PDGF-TNPI allows a different approach for approximately truncating memory when the Hamiltonian is time-independent. This method utilizes the Green’s function for L step propagation, G_L . We apply this to the density matrix $\tilde{\rho}(k\Delta t)$ to get $\tilde{\rho}((k+L)\Delta t)$ for all k . We call this scheme the Markovian iteration TNPI scheme (MTNPI). Of course, we use the exact $\tilde{\rho}(k\Delta t)$ when $k \leq L$, and thereafter, we use the reduced density matrices predicted by MTNPI. This scheme misses out on some interactions in the canonical iteration scheme, and consequently introduces additional spurious memory. However, if the increased memory can be spanned, the iteration is just a sequence of matrix-vector multiplications, and hence very fast. Even when memory is not converged, this method results in computationally cheap dynamics that is quite physically insightful. This computational advantage becomes especially important when the total time-scale of the dynamics far exceeds the length of the non-Markovian memory.

Please note that while for simplicity the entire development in this section has been done in terms of a bilinearly coupled bath that interacts with the “position” operator of the system, this is not a necessary restriction. The formalism of Feynman-Vernon influence functionals is general, and consequently PDGF-TNPI can also be extended to deal with other couplings. The more general expressions are presented in Appendix A.

III. RESULTS

We will now apply PDGF-TNPI to a large variety of illustrative examples. This section is organized as follows: first, we benchmark the method on two-level systems against iterative QuAPI. We try to understand the behavior of the bond dimensions and convergence in general. We show that PDGF-TNPI can simulate dynamics which were previously only treated with more advanced path integral techniques like QCPI or blip-summed path integrals (BSPI) [33, 34]. Then, we apply PDGF-TNPI to two realistic applications: a charge transfer example and excitonic dynamics in a dimer. For the charge transfer, using a combination of rate theory and direct dynamics, we try to understand the essential physics, whereas for the excitonic dynamics, we are able to converge the dynamics directly. Finally, we show examples of applying PDGF-TNPI to multilevel systems like molecular wires.

Before continuing to the results, a brief mention of the convergence parameters is in order. Apart from the standard time step (Δt) and memory length (L) associated with iterative path integral methods, PDGF-TNPI has two additional controllable parameters: the maximum allowable bond dimension (M), and the truncation threshold (χ). While the precise meaning of the truncation threshold depends of the exact nature of the compression algorithm used, for the most part it can be thought of as a SVD truncation, where any singular values smaller than the given threshold are discarded. These four parameters are interrelated, therefore, the convergence is ultimately a search procedure to find the combination that gives the correct dynamics at the least cost. For simplicity, we generally have not explicitly constrained the maximum bond dimension.

A. Two-level systems

Two-level systems (TLS) are some of the most commonly studied model systems in quantum dynamics. They are relatively simple and yet support a surprisingly rich array of dynamics. As the name implies, the system is described by a Hamiltonian with 2 states:

$$\hat{H}_0 = \sum_{j=1}^2 \epsilon_j |\sigma_j\rangle\langle\sigma_j| - \hbar\Omega (|\sigma_1\rangle\langle\sigma_2| + |\sigma_2\rangle\langle\sigma_1|), \quad (33)$$

where $|\sigma_1\rangle$ and $|\sigma_2\rangle$ are eigenstates of the system's position operator, \hat{s} , i.e., $\hat{s}|\sigma_j\rangle = \sigma_j|\sigma_j\rangle$; throughout this subsection, this pair of eigenvalues, $\{\sigma_1, \sigma_2\}$, will be referred to as the system's coordinates. Additionally, the position dependent energies are defined as $\epsilon_1 = \epsilon$ and $\epsilon_2 = -\epsilon$. With this model, the key parameters are the asymmetry, ϵ , and the tunneling splitting of $2\hbar\Omega$. All the examples in this subsection use Eq. (33) as the Hamiltonian for the isolated system.

1. Benchmark calculations

For the benchmark calculations, we track the population decay of the system. More specifically, we simulate $\langle 1|\tilde{\rho}(t)|1\rangle$, where $\langle 1|\tilde{\rho}(0)|1\rangle = 1$. The system is taken to be coupled bi-linearly with a harmonic bath as described by Eq. (2), with the spectral density having the Ohmic form

$$J(\omega) = \frac{\pi}{2} \hbar \xi \omega \exp\left(-\frac{\omega}{\omega_c}\right). \quad (34)$$

Here, ξ is the dimensionless Kondo parameter that characterizes the system-bath coupling, and ω_c is the cutoff frequency of the bath. To keep these calculations general, the parameters are given in terms of Ω .

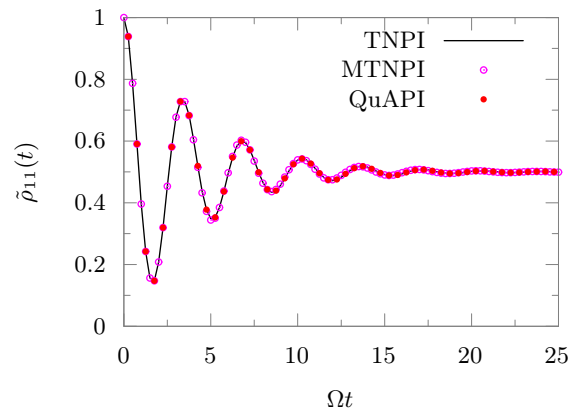


FIG. 3. Comparison with QuAPI for typical spin-boson. Bath is characterized by $\hbar\Omega\beta = 5$, $\omega_c = 7.5\Omega$, $\xi = 0.1$, $\chi = 10^{-15}$.

In Fig. 3, we compare fully converged PDGF-TNPI results with QuAPI for a system interacting weakly with a cold, fast harmonic bath, as represented by $\hbar\Omega\beta = 5$, $\omega_c = 7.5\Omega$ and $\xi = 0.1$. The system's coordinates are $\{1, -1\}$. Because there are no additional approximations, both PDGF-TNPI and QuAPI converge with exactly the same $\Omega\Delta t = 0.25$ and $L = 8$. We show the converged results for MTNPI done at $L = 15$. Despite the additional spurious memory introduced by the simplified MTNPI propagation scheme, the basic physics is still reproduced.

Before showing more computationally intensive examples, let us analyze the growth of the bond dimension with the memory length L and the cutoff χ for the simple case of Fig. 3. In Table I, we show the average and maximum bond dimensions corresponding to calculations with particular memory length, L . Even with a minimal value of $\chi > 0$, there is a dramatic reduction of the bond dimensions. Since the cost of the MPO-MPS application goes as the cube of the typical MPS bond dimension, setting $\chi = 0$ results in a calculation that is possibly even more costly than QuAPI. However, even the smallest amount of filtration dramatically reduces the cost of the calculation. If we consider the the growth of the average and maximum bond dimensions between different

L	M_0	$M_{10^{-15}}$	$M_{10^{-10}}$	$M_{10^{-5}}$	#paths
2	4.00, 4	4.00, 4	4.00, 4	4.00, 4	16
4	8.80, 16	8.00, 16	7.20, 14	4.00, 4	256
6	24.57, 64	14.43, 35	10.28, 19	5.14, 6	4096
8	76.00, 256	21.11, 48	12.78, 22	5.22, 6	65536
10	238.27, 1024	26.54, 54	14.00, 21	5.45, 6	1048576
12	840.31, 4096	31.08, 57	14.61, 20	5.54, 6	16777216

TABLE I. Growth of average and maximum bond dimension at $\Omega t = 10$ for different χ (as denoted by M_χ). The number of system paths in a typical path integral calculation and the bond dimensions at $\chi = 0$ are also shown for comparison.

values of L , we notice that once the memory length is spanned ($L = 8$ in this case), the rate at which the bond dimension increases becomes smaller. We believe this to be a signature of spanning the full memory length. Once the memory of the problem under consideration is spanned, the MPS compression does an excellent job of filtering out the additional and unnecessary data that results from increasing L any further.

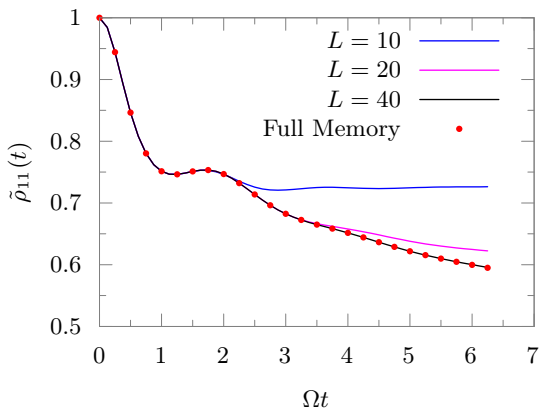


FIG. 4. Simulation with very long non-Markovian memory: $\epsilon = 0$, $\hbar\Omega\beta = 1$, $\omega_c = \Omega$, $\xi = 2$.

In Fig. 4, we consider a symmetric TLS ($\epsilon = 0$) strongly coupled ($\xi = 2$) to a sluggish bath ($\omega_c = \Omega$). The system's coordinates are $\{0, -2\}$, i.e., the bath is initially equilibrated to the populated state of the system. Here, $\Omega\Delta t = 0.125$ and $\chi = 10^{-15}$. The strong coupling and sluggish bath imply that the non-Markovian memory is quite long. Walters and Makri [28] have shown that in this parameter regime iterative QuAPI can not converge the dynamics, and either QCPI or BSPI is required to access the relevant memory lengths. It is interesting to note that with PDGF-TNPI, owing to the compressions enabled by the MPS representation, we can converge the dynamics directly. The convergence being reached at almost full memory. Note that for the full memory calculations of 50 time steps, an equivalent QuAPI simulation would effectively sum over 4^{50} paths or roughly 10^{30} paths, which is computationally infeasible.

We also simulate the full memory dynamics using var-

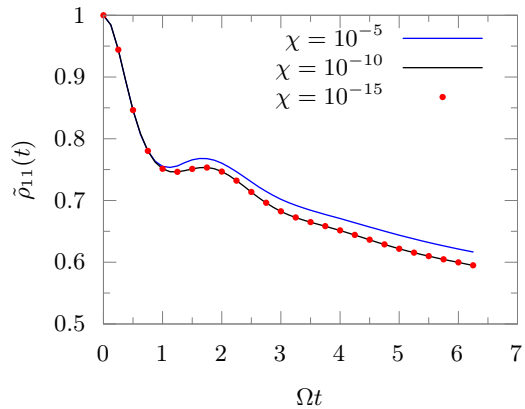


FIG. 5. Dynamics for different values of χ when M is left unconstrained. Parameters same as Fig. 4. These are full memory calculations.

ious cutoffs in Fig. 5. Even at a fairly large cutoff of $\chi = 10^{-5}$, though the dynamics is not converged, the key features are preserved. It is worth noting that although the maximum bond dimension, with $\chi = 10^{-5}$, is never greater than eight, the resulting error is smaller than that produced from a memory truncation of $L = 10$. Given how the bond truncation works when applying a MPO to a MPS, even with relatively large values of χ , unitarity of propagation is preserved and consequently, the trace is conserved.

2. Realistic applications of spin-boson model

The compressed representation enabled by PDGF-TNPI allows us to span substantially longer memories than before. This makes it possible to use PDGF-TNPI to, at least qualitatively, understand the physics of realistic systems. As the first example, consider the charge transfer in the ferrocene-ferrocenium complex in hexane as a solvent. This system was studied using QCPI by one of us [55]. It was shown that the harmonic bath results match the fully atomistic results really well. We apply PDGF-TNPI to understand the dynamics qualitatively using only short calculations that can be run on extremely modest computational resources.

The system is described by a symmetric TLS Hamiltonian, where $\hbar\Omega = 32 \text{ cm}^{-1}$ and $\epsilon = 0$. As in Eq. (2), the system is coupled bi-linearly to the bath, which is initially equilibrated with the donor state. The spectral density of the harmonic bath with a reorganization energy of 36 meV [55] is shown in Fig. 6. It is extremely challenging to converge the full dynamics using the basic PDGF-TNPI framework outlined here because of long memory times, however, we can quite easily converge the initial decay of the population. It is the presence of classical trajectories in QCPI that allows for accelerated convergence with respect to memory length. Such improve-

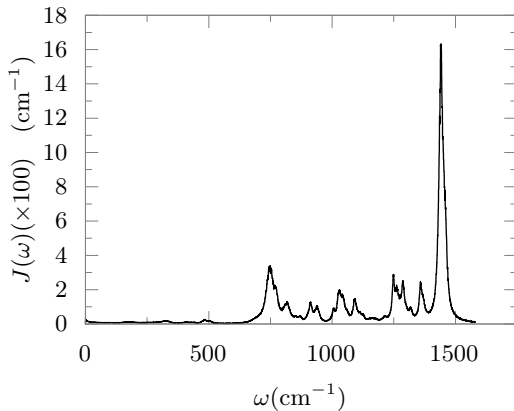


FIG. 6. Spectral density for hexane interacting with ferrocene-ferrocenium.

ments can, in principle, be added into PDGF-TNPI, and will be the subject of future research. Here we use the basic PDGF-TNPI framework outlined in this paper.

For reactions with long time-scales, rate theory can often be used to gain valuable insights. Quantum mechanical rates are typically related to equilibrium correlation functions involving the flux operator, $\hat{F} = \frac{i}{\hbar} [\hat{H}_0, \hat{h}]$ where $\hat{h} = |1\rangle\langle 1|$ is the projector on the donor state, $|1\rangle$ [56–60]. Since the equilibrium of a system coupled to a solvent can often be challenging to compute, it has also been shown that the same information can be obtained from the non-equilibrium flux function [61], which also happens to be related to the instantaneous time-derivative of the donor population. In Fig. 7, we show the short-time dynamics of both the donor population, $\tilde{\rho}_{11}(t)$, and the donor flux, $F(t) = \frac{d\tilde{\rho}_{11}}{dt} = \text{Tr}(\tilde{\rho}(t)\hat{F})$, as calculated by PDGF-TNPI. The simulation was run at $T = 300$ K. Convergence was reached with a time-step of $\Delta t \approx 12$ fs. These simulations are full memory and the truncation cutoff used was $\chi \approx 0$. In this case, because of its complexity, we limited the maximum bond dimension to $M = 1000$. A laptop with a total RAM of 8 GB was used for the computation. With access to larger computer memory, it might well be possible to converge the full dynamics directly with PDGF-TNPI. (It is instructive to note that the converged QCPI calculations were run on the BlueWaters supercomputing facility.)

The population has not decayed to equilibrium within the first 300 fs. However, a lot of information about the dynamics can be gleaned from the flux function (blue curve). If rate theory had been valid, and a slow exponential decay were to govern the dynamics, then the flux function should plateau at the rate after some transients. We see that the flux function shows dramatic changes implying that the transients are not completely over. Combining this with the fact that the amount of population decay that we see is not insignificant, we can conclude that the dynamics is not purely exponential. A

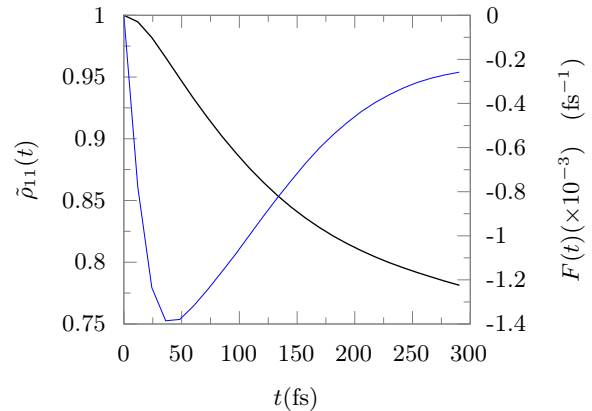


FIG. 7. Population of donor state (black line, left axis) and flux of the donor state (blue line, right axis) as a function of time.

“dominant” $\frac{1}{e}$ -time of ~ 720 fs can be obtained from the maximum flux out of the donor state. This value agrees with the reported $\frac{1}{e}$ -time of 830 fs calculated from the full QCPI dynamics. The flux curve also shows a significant slowing down of the dynamics in a non-exponential manner. Consequently, traditional equilibrium rate theory would give incorrect rates and predict much longer time-scales. At longer times, the donor flux seems to be reaching a plateau at around 0.00025 fs^{-1} which would give a $\frac{1}{e}$ -time of ~ 4 ps for the slow decay at long times. This value also agrees with the $\frac{1}{e}$ -time reported by Walters and Makri [55] corresponding to the long-time exponential behavior.

Though the method can be readily extended to larger systems, let us, now, turn our attention to exciton transfer in a dimer. This can be considered the simplest illustrative example of an exciton transfer. Restricting ourselves to the single-exciton Frenkel subspace, we have a two-level description for the system where $|\sigma_1\rangle$ corresponds to the first monomer being in the excited state and the second in the ground state; and $|\sigma_2\rangle$ corresponds to the second monomer being in the excited state and the first in the ground state. The vibrational degrees of freedom of each of the monomers produce a dissipative bath. The Hamiltonian of the bath and its interaction with the system is now given by

$$\hat{H}_b = \sum_{j,b} \frac{p_{jb}^2}{2m_{jb}} + \frac{1}{2} m_{jb} \omega_{jb}^2 \left(x_{jb} - \frac{c_{jb} \hat{V}_j}{m_{jb} \omega_{jb}^2} \right)^2 \quad (35)$$

where the b^{th} vibrational mode associated with the j^{th} monomer has a frequency of ω_{jb} and coupling constant of c_{jb} . Additionally, $\hat{V}_j = |\sigma_j\rangle\langle \sigma_j|$ is the projector on to state where the j^{th} monomer is excited. This coupling to the system captures the shift of the Born-Oppenheimer surfaces of the localized vibrations between the ground and the excited electronic states of the monomer.

Since the two monomers are identical molecules, the

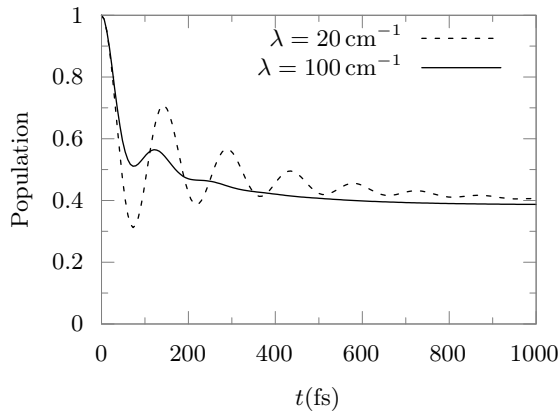


FIG. 8. Excitonic dynamics in a dimer ($\epsilon = 50 \text{ cm}^{-1}$, $\hbar\Omega = -100 \text{ cm}^{-1}$) with a Drude bath with $\gamma = 53.08 \text{ cm}^{-1}$ at $T = 300 \text{ K}$.

spectral densities for the localized molecular vibrations are taken to be identical for both the baths. While PDGF-TNPI is able to handle discrete rigid vibrations directly, for the current tests we follow Ishizaki and Fleming [62] and assume that the bath is described by a Drude spectral density,

$$J(\omega) = 2\lambda\gamma\frac{\omega}{\omega^2 + \gamma^2}, \quad (36)$$

where λ is the reorganization energy and γ is the cutoff frequency. Figure 8 shows the dynamics of the population corresponding to $|\sigma_1\rangle$ in the excitonic dimer defined by $\hbar\Omega = -100 \text{ cm}^{-1}$, $\epsilon = 50 \text{ cm}^{-1}$ and $\gamma = 53.08 \text{ cm}^{-1}$ at two different values of reorganization energies 20 cm^{-1} and 100 cm^{-1} . These simulations were performed at room temperature, i.e., $T = 300 \text{ K}$. A time step of $\Delta t = 6.05 \text{ fs}$ was used with a memory length of $L = 80$ and a truncation threshold of $\chi = 10^{-10}$. The results are same as the ones reported by Ishizaki and Fleming.

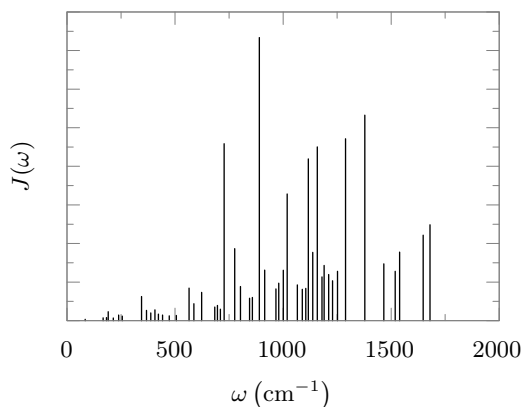


FIG. 9. Vibrational spectral density for a bacteriochlorophyll molecule in arbitrary units.

Though, till now, we discussed the dynamics corre-

sponding to the Drude spectral density, chlorophyll, being a rigid monomer, has a much more structured, discrete vibrational spectral density. The detailed impact of such structured vibrations on the dynamics cannot be captured by using model spectral densities. Figure 9 shows the spectral density obtained from the Huang-Rhys factors reported by Rätsep *et al.* [63]. This vibrational bath has already been used to study the quantum dynamics of a bacteriochlorophyll (BChl) dimer using QCPI [64] and for longer BChl chains and rings [65] using modular path integral [66–68].

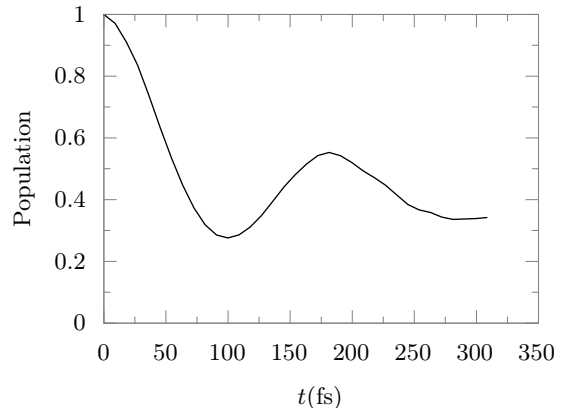


FIG. 10. Excitonic dynamics in a dimer with the rigid, structured bath given in Fig. 9. The system Hamiltonian is the same as used in Fig. 8.

The dynamics of the same excitonic dimer system under this structured vibrational bath is shown in Fig. 10 using a time step of $\Delta t = 9.07 \text{ fs}$. A truncation cutoff of $\chi = 10^{-10}$ was used. For this simulation, we did not truncate memory. We note that there are certain differences between Fig. 10 and Fig. 8. Most prominently, there are “uneven” properties to the dynamics such as the small shoulder-like features around 225 fs and 250 fs. These features are due to the absence of a continuous manifold of vibrational states guaranteed by a model spectral density. Generally, the presence of many ro-translational modes lead to such continuous spectral densities. However, since, for simplicity, we are dealing with two isolated bacteriochlorophyll molecules, the vibrational modes are discontinuous. This is, of course, not the whole story. The presence of a protein scaffolding would lead to a bath common to all the monomers with many ro-translational modes. In principle, we should be able to include such common baths with PDGF-TNPI as well.

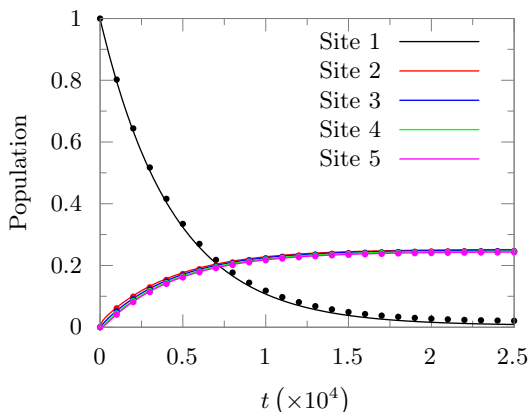
B. Multilevel systems

Finally, we explore the dynamics of systems with more than two levels. As an application, let us consider a molecular wire for charge transport. The system is de-

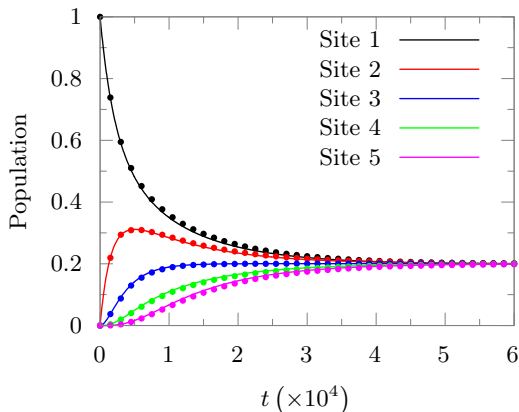
scribed by a tight-binding Hamiltonian with N sites:

$$\hat{H}_0 = \sum_{1 \leq j \leq D} \epsilon_j |\sigma_j\rangle \langle \sigma_j| - \hbar V \sum_{1 \leq j < D} (|\sigma_j\rangle \langle \sigma_{j+1}| + |\sigma_{j+1}\rangle \langle \sigma_j|) \quad (37)$$

The sites are separated by unit distance. Therefore, the site locations are given by $\hat{s}|\sigma_j\rangle = (j-1)|\sigma_j\rangle$ for all $1 \leq j \leq D$. The process is started with the $j=1$ site being populated. The bath is initially equilibrated with this $j=1$ site. The presence of such a global bath prevents use of more recent methods like modular path integrals [66, 67] that are based on the separability of local environments. Following Lambert and Makri [69], we choose $V = 0.025$ and $\epsilon_1 = 1$. For all other sites, $1 < j \leq D$, $\epsilon_j = 0$. The bath is characterized by the Ohmic spectral density defined in Eq. (34) with $\omega_c = 4$, $\xi = 0.12$.



(a) Cold bath, $\beta = 2$. Converged memory length $L = 24$. MTNPI iteration with $L = 320$.



(b) Hot bath, $\beta = 0.01$. Converged memory length $L = 10$. MTNPI iteration with $L = 30$.

FIG. 11. Population dynamics of a molecular wire of chain of length $D = 5$ described by Eq. (37). Lines represent the MTNPI iteration scheme. Points represent the rigorously correct algorithm.

In Fig. 11, we show the dynamics of the population

for a molecular wire of length, $D = 5$ at two different inverse temperatures, $\beta = 2$ (Fig. 11 (a)) and $\beta = 0.01$ (Fig. 11 (b)). A cutoff of $\chi = 10^{-7}$ was used for the low temperature calculation, and for the high temperature simulation $\chi = 10^{-12}$ was used. For both cases, a time-step of $\Delta t = 0.2$ was used. Because of the structure of this problem, even with such a small cutoff, the maximum bond dimension was stable at $D^2 = 25$ for both the temperatures, and the average bond dimension decreases to 13.96 for the low temperature case and 15.18 for the high temperature case. The higher temperature bath tends to lead to a sequential transfer of the excess charge, whereas the colder bath leads to an almost simultaneous transfer of population onto all the acceptor sites. The MTNPI scheme is quite accurate: we get the basic features of the dynamics for the low temperature case, and quantitative agreement with the correct dynamics for the high temperature simulation. Though it requires much higher memory lengths to converge, the net time required for the full simulation is orders of magnitude less than the canonical algorithm for iteration. This is because, in the MTNPI scheme, the full complexity of the longer memory only affects the within-memory portion of the simulation. Thereafter, MTNPI abandons the PDGF and just performs tensor contractions of the form $\tilde{\rho}(t+L\Delta t) = G(L\Delta t)\tilde{\rho}(t)$ along an index with dimensionality of D^2 . In contrast, for the canonical and rigorously correct scheme of iteration, the computational complexity remains approximately constant once in the iterative regime of the dynamics. This becomes a significant bottleneck when the iterative regime consists of hundreds of thousands of time steps.

The effective asymmetry in the low temperature case possibly leads the spurious MTNPI memory to increase very rapidly. For the high temperature simulation, the asymmetry is not important on the scale of the thermal energy, and consequently, the spurious MTNPI memory is not as long compared to the converged memory of the full PDGF-TNPI calculation. Because MTNPI propagates the reduced density matrix of the system from time t to $t + L\Delta t$ with an effective Green's function, it assumes that the bath and the system are uncorrelated at time t . We hypothesize that this implicit assumption performs poorly when the asymmetry of the system is important. This would be consistent with what was observed in QCPI [28]. Though this limitation can probably be dealt with in a computationally efficient manner by augmenting MTNPI with the ability to update the Green's function to be used in a dynamically consistent manner, it is not important for the purposes of this example.

IV. CONCLUSION

System-solvent decomposition is a ubiquitous approach to quantum dynamics in condensed phase where the quantum effects are primarily limited to a low-dimensional subspace. We have presented a tensor net-

work approach to simulating such systems using the quasi-adiabatic propagators and Feynman-Vernon influence functionals. This brings a novel perspective and decomposition to a well-established problem.

Tensor networks utilize certain symmetries in the tensors to obtain highly efficient “factorized” representations. The observation that the entanglement between time-points cannot span temporal lengths greater than that of the non-Markovian memory associated with the bath response function suggests extremely compact matrix-product state representation of the path-dependent Green’s function. (It should be noted here that probably many other TNPI representations are possible in addition to the current PDGF-TNPI. One of us is developing a different TNPI formulation.) There are well-established techniques for SVD-based and variational optimizations of MPSs that lead to further automatic compression of the PDGF. This makes it possible to simulate problems with longer non-Markovian memory lengths and with larger system sizes than earlier possible, without sacrificing the rigorous nature of QuAPI. The structure of PDGF-TNPI suggests an extremely simple and powerful approximate scheme for computing the reduced density matrix beyond the memory length. We call this approximate scheme the Markovian iteration scheme (MTNPI). MTNPI reduces the computational complexity of each step to the cost of a single tensor contraction involving indices with dimension D^2 . Though MTNPI introduces spurious memory, using it is especially useful when the total time of propagation far exceeds the memory time. Because PDGF-TNPI already allows us to access much longer memories than earlier possible, it is not very difficult to span the increased MTNPI memory as well.

After testing the new PDGF-TNPI framework against benchmark spin-boson simulations, we applied it to study two realistic applications. First, we used a combination of direct dynamics and rate theory to understand the physics of charge transfer in ferrocene-ferrocenium solvated in hexane. These calculations were performed on extremely modest computers and the time-scales that we obtained were consistent with those found in previous QCPI simulations. As a second example of a two-level system, we used PDGF-TNPI to simulate the exciton dynamics of a chlorophyll dimer with both a Drude bath and a bath of discrete vibrations. We reproduced results obtained by Ishizaki and Fleming [62]. The bath of discrete vibrations leaves some unusual features on the dynamics as compared to the standard model spectral densities. Apart from two-level systems, we also applied PDGF-TNPI to simulate the dynamics of a charge transfer in a molecular wire coupled to global solvents. In the molecular wire examples, the computational efficiency of MTNPI could truly be leveraged because the memory length required to be spanned was much shorter than the total time of propagation. Though quite accurate otherwise, MTNPI seems to perform comparatively less efficiently when the asymmetry in the system is impor-

tant. We have postulated a possible solution, that we would explore in the future to make general applications with MTNPI even more accurate.

Through all these applications, we have demonstrated the wide-ranging applicability of PDGF-TNPI to a variety of problems using only modest computational resources. Future applications would focus on simulation of spectra in various systems such as photosynthetic complexes and an analysis of the effect of a structured spectral density of the bath on these spectra. While the current examples of the excitonic dimer incorporate a local bath, it is possible to incorporate effects of a global rotational solvent. This, along with atomistic simulations with classical trajectories, would allow us to evaluate the accuracy of linear response in modeling the protein backbones.

Since PDGF-TNPI is still a path integral technique, many developments in path integrals involving improved reference propagators [27] and harmonic back reaction [70] to cheaply include anharmonic effects via classical trajectories can be transparently implemented in PDGF-TNPI. Additionally, a different and extremely promising avenue of exploration relates to application of PDGF-TNPI to extended systems. Simulations of energy and charge transfer along long molecular chains and aggregates are of particular interest. We have already demonstrated applications of the PDGF-TNPI framework introduced here to small multi-state systems interacting with a global solvent. However, for longer, extended systems with short-range interaction between sites, the structure of PDGF-TNPI can also be augmented to decompose the system as a further optimization.

Future development would follow two broad avenues: incorporation of anharmonic and atomistic environments using classical trajectories, and development of spatial decomposition using tensor networks to efficiently work with extended systems containing relatively localized short-ranged interactions. We believe that PDGF-TNPI is a potentially viable framework for developing methods to study the dynamics of several important condensed phase problems.

ACKNOWLEDGMENTS

We thank Nancy Makri for introducing us to the world of quantum dynamics in general and real time path integrals in particular. A. B. acknowledges the support of the Computational Chemical Center: Chemistry in Solution and at Interfaces funded by the US Department of Energy under Award No. DE-SC0019394. P.W. acknowledges the Miller Institute for Basic Research in Science for funding.

Appendix A: Influence Functional for Localized Baths

In Sec. II, we discussed the method primarily for a harmonic bath bilinearly coupled to the “position” operator, \hat{s} , of the system. However, the influence functionals can be used in a straightforward manner with multiple baths that couple to different system operators. Here we list the basic equations and changes to the algorithm required to make PDGF-TNPI work with the more general bath. Even for this case, further optimizations are possible that are not described here as they are not the focus of this paper.

Suppose after QuAPI splitting, the Hamiltonian for independent baths acting through separate system operators is given as

$$\hat{H}_b = \sum_{j,b} \frac{p_{jb}^2}{2m_{jb}} + \frac{1}{2} m_{jb} \omega_{jb}^2 \left(x_{jb} - \frac{c_{jb} \hat{V}_j}{m_{jb} \omega_{jb}^2} \right)^2. \quad (\text{A1})$$

Here for each of the system operators indexed by j , there is an independent bath with modes indexed by b . The frequency and coupling of the b^{th} mode of the j^{th} bath is ω_{jb} and c_{jb} respectively. The j^{th} bath interacts with the system through \hat{V}_j . For path integral calculations, we want to work in a representation of the system where \hat{V}_j is diagonal for all j .

The independent baths are specified by the spectral

densities

$$J_j(\omega) = \frac{\pi}{2} \sum_b \frac{c_{jb}^2}{m_{jb} \omega_{jb}} \delta(\omega - \omega_{jb}). \quad (\text{A2})$$

which lead to separate η -coefficients for each of the baths. The η -coefficient for the j^{th} bath is denoted by η^j . These independent, local baths feature most prominently in descriptions of the local vibrations of monomers in exciton transfer complexes and chromophores.

The only change to the dynamics happens through a change in the influence functional, which becomes a product of all the influence functionals corresponding to the different baths. More specifically, Eq. (8) would now be replaced by

$$F[\{s_n^\pm\}] = \prod_j \exp \left(-\frac{1}{\hbar} \sum_{0 \leq k \leq N} \Delta V_{jk} \sum_{0 \leq k' \leq k} \left(\text{Re}(\eta_{kk'}^j) \Delta V_{jk'} + 2i \text{Im}(\eta_{kk'}^j) \bar{V}_{jk'} \right) \right) \quad (\text{A3})$$

where $\Delta V_{jk} = V_j(s_k^+) - V_j(s_k^-)$ and $\bar{V}_{jk} = \frac{V_j(s_k^+) + V_j(s_k^-)}{2}$.

Therefore, instead of having one IF MPO, now there would be as many IF MPOs as there are independent baths. The total IF MPO is defined to be the product of all the individual ones.

-
- [1] L. Zhang, M. Chen, X. Wu, H. Wang, W. E, and R. Car, Deep neural network for the dielectric response of insulators, *Phys. Rev. B* **102**, 1 (2020).
- [2] M. H. Beck, A. Jäckle, G. A. Worth, and H.-D. Meyer, The multiconfiguration time-dependent Hartree (MCTDH) method: A highly efficient algorithm for propagating wavepackets, *Phys. Rep.* **324**, 1 (2000).
- [3] H. Wang and M. Thoss, Multilayer formulation of the multiconfiguration time-dependent Hartree theory, *J. Chem. Phys.* **119**, 1289 (2003).
- [4] S. R. White and A. E. Feiguin, Real-Time Evolution Using the Density Matrix Renormalization Group, *Phys. Rev. Lett.* **93**, 076401 (2004).
- [5] U. Schollwöck, The density-matrix renormalization group, *Rev. Mod. Phys.* **77**, 259 (2005).
- [6] H. Ma, Z. Luo, and Y. Yao, The time-dependent density matrix renormalisation group method, *Mol. Phys.* **116**, 854 (2018).
- [7] J. Liu and W. H. Miller, Using the thermal Gaussian approximation for the Boltzmann operator in semiclassical initial value time correlation functions, *J. Chem. Phys.* **125**, 224104 (2006).
- [8] J. Liu and W. H. Miller, Real time correlation function in a single phase space integral beyond the linearized semiclassical initial value representation, *J. Chem. Phys.* **126**, 234110 (2007).
- [9] R. Gelabert, X. Giménez, M. Thoss, H. Wang, and W. H. Miller, A Log-Derivative Formulation of the Prefactor for the Semiclassical Herman-Kluk Propagator†, *J. Phys. Chem. A* **104**, 10321 (2000).
- [10] R. Gelabert, X. Giménez, M. Thoss, H. Wang, and W. H. Miller, Semiclassical description of diffraction and its quenching by the forward-backward version of the initial value representation, *J. Chem. Phys.* **114**, 2572 (2001).
- [11] V. Guallar, V. S. Batista, and W. H. Miller, Semiclassical molecular dynamics simulations of excited state double-proton transfer in 7-azaindole dimers, *J. Chem. Phys.* **110**, 9922 (1999).
- [12] J. Cao and G. A. Voth, The formulation of quantum statistical mechanics based on the Feynman path centroid density. I. Equilibrium properties, *J. Chem. Phys.* **100**, 5093 (1994).
- [13] J. Cao and G. A. Voth, The formulation of quantum statistical mechanics based on the Feynman path centroid density. II. Dynamical properties, *J. Chem. Phys.* **100**, 5106 (1994).
- [14] I. R. Craig and D. E. Manolopoulos, Quantum statistics and classical mechanics: Real time correlation functions from ring polymer molecular dynamics, *J. Chem. Phys.* **121**, 3368 (2004).

- [15] S. Habershon, B. J. Braams, and D. E. Manolopoulos, Quantum mechanical correlation functions, maximum entropy analytic continuation, and ring polymer molecular dynamics, *J. Chem. Phys.* **127**, 174108 (2007).
- [16] M. Rossi, M. Ceriotti, and D. E. Manolopoulos, How to remove the spurious resonances from ring polymer molecular dynamics, *J. Chem. Phys.* **140**, 234116 (2014).
- [17] N. Ananth, C. Venkataraman, and W. H. Miller, Semi-classical description of electronically nonadiabatic dynamics via the initial value representation, *J. Chem. Phys.* **127**, 084114 (2007).
- [18] R. Liang, S. J. Cotton, R. Binder, R. Hegger, I. Burghardt, and W. H. Miller, The symmetrical quasi-classical approach to electronically nonadiabatic dynamics applied to ultrafast exciton migration processes in semiconducting polymers, *J. Chem. Phys.* **149**, 044101 (2018).
- [19] M. S. Church, T. J. H. Hele, G. S. Ezra, and N. Ananth, Nonadiabatic semiclassical dynamics in the mixed quantum-classical initial value representation, *J. Chem. Phys.* **148**, 102326 (2018).
- [20] J. C. Tully and R. K. Preston, Trajectory Surface Hopping Approach to Nonadiabatic Molecular Collisions: The Reaction of H^+ with D_2 , *J. Chem. Phys.* **55**, 562 (1971).
- [21] D. S. Sholl and J. C. Tully, A generalized surface hopping method, *J. Chem. Phys.* **109**, 7702 (1998).
- [22] J. C. Tully, Perspective: Nonadiabatic dynamics theory, *J. Chem. Phys.* **137**, 22A301 (2012).
- [23] G. Miao, N. Bellonzi, and J. Subotnik, An extension of the fewest switches surface hopping algorithm to complex Hamiltonians and photophysics in magnetic fields: Berry curvature and “magnetic” forces, *J. Chem. Phys.* **150**, 124101 (2019).
- [24] R. Kapral and G. Ciccotti, Mixed quantum-classical dynamics, *J. Chem. Phys.* **110**, 8919 (1999).
- [25] R. Lambert and N. Makri, Quantum-classical path integral. I. Classical memory and weak quantum nonlocality, *J. Chem. Phys.* **137**, 22A552 (2012).
- [26] R. Lambert and N. Makri, Quantum-classical path integral. II. Numerical methodology, *J. Chem. Phys.* **137**, 22A553 (2012).
- [27] T. Banerjee and N. Makri, Quantum-classical path integral with self-consistent solvent-driven reference propagators, *J. Phys. Chem. B* **117**, 13357 (2013).
- [28] P. L. Walters and N. Makri, Iterative quantum-classical path integral with dynamically consistent state hopping, *J. Chem. Phys.* **144**, 044108 (2016).
- [29] R. P. Feynman and F. L. Vernon, The theory of a general quantum system interacting with a linear dissipative system, *Ann. Phys. (N. Y.)* **24**, 118 (1963).
- [30] N. Makri, The Linear Response Approximation and Its Lowest Order Corrections: An Influence Functional Approach, *J. Phys. Chem. B* **103**, 2823 (1999).
- [31] N. Makri and D. E. Makarov, Tensor propagator for iterative quantum time evolution of reduced density matrices. I. Theory, *J. Chem. Phys.* **102**, 4600 (1995).
- [32] N. Makri and D. E. Makarov, Tensor propagator for iterative quantum time evolution of reduced density matrices. II. Numerical methodology, *J. Chem. Phys.* **102**, 4611 (1995).
- [33] N. Makri, Exploiting classical decoherence in dissipative quantum dynamics: Memory, phonon emission, and the blip sum, *Chem. Phys. Lett.* **593**, 93 (2014).
- [34] N. Makri, Blip decomposition of the path integral: Exponential acceleration of real-time calculations on quantum dissipative systems, *J. Chem. Phys.* **141**, 134117 (2014).
- [35] N. Makri, Small matrix disentanglement of the path integral: Overcoming the exponential tensor scaling with memory length, *J. Chem. Phys.* **152**, 041104 (2020).
- [36] N. Makri, Small Matrix Path Integral for System-Bath Dynamics, *J. Chem. Theory Comput.* **16**, 4038 (2020).
- [37] S. R. White, Density matrix formulation for quantum renormalization groups, *Phys. Rev. Lett.* **69**, 2863 (1992).
- [38] U. Schollwöck, The density-matrix renormalization group in the age of matrix product states, *Ann. Phys. (N. Y.)* **326**, 96 (2011).
- [39] U. Schollwöck, The density-matrix renormalization group: A short introduction, *Philos. Trans. R. Soc. A Math. Phys. Eng. Sci.* **369**, 2643 (2011).
- [40] E. M. Stoudenmire, L. O. Wagner, S. R. White, and K. Burke, One-Dimensional Continuum Electronic Structure with the Density-Matrix Renormalization Group and Its Implications for Density-Functional Theory, *Phys. Rev. Lett.* **109**, 056402 (2012).
- [41] E. Stoudenmire and S. R. White, Studying Two-Dimensional Systems with the Density Matrix Renormalization Group, *Annu. Rev. Condens. Matter Phys.* **3**, 111 (2012).
- [42] R. Orús, A practical introduction to tensor networks: Matrix product states and projected entangled pair states, *Ann. Phys. (N. Y.)* **349**, 117 (2014).
- [43] G. Vidal, Entanglement Renormalization, *Phys. Rev. Lett.* **99**, 220405 (2007).
- [44] G. Vidal, Class of quantum Many-Body states that can be efficiently simulated, *Phys. Rev. Lett.* **101**, 1 (2008).
- [45] ITensor Library (version 3.0.0), ITensor Libr. (version 3.0.0) <https://itensor.org>.
- [46] A. Caldeira and A. Leggett, Path integral approach to quantum Brownian motion, *Phys. A Stat. Mech. its Appl.* **121**, 587 (1983).
- [47] S. Nakajima, On Quantum Theory of Transport Phenomena, *Prog. Theor. Phys.* **21**, 659 (1959).
- [48] R. Zwanzig, Ensemble method in the theory of irreversibility, *J. Chem. Phys.* **33**, 1338 (1960).
- [49] Q. Shi and E. Geva, A new approach to calculating the memory kernel of the generalized quantum master equation for an arbitrary system–bath coupling, *J. Chem. Phys.* **119**, 12063 (2003).
- [50] A. Montoya-Castillo and D. R. Reichman, Approximate but accurate quantum dynamics from the Mori formalism: I. Nonequilibrium dynamics, *J. Chem. Phys.* **144**, 184104 (2016).
- [51] A. Kelly, A. Montoya-Castillo, L. Wang, and T. E. Markland, Generalized quantum master equations in and out of equilibrium: When can one win?, *J. Chem. Phys.* **144**, 184105 (2016).
- [52] L. Kidon, H. Wang, M. Thoss, and E. Rabani, On the memory kernel and the reduced system propagator, *J. Chem. Phys.* **149**, 104105 (2018).
- [53] S. Chatterjee and N. Makri, Real-Time Path Integral Methods, Quantum Master Equations, and Classical vs Quantum Memory, *J. Phys. Chem. B* **123**, 10470 (2019).
- [54] S. Paekel, T. Köhler, A. Swoboda, S. R. Manmana, U. Schollwöck, and C. Hubig, Time-evolution methods for matrix-product states, *Ann. Phys. (N. Y.)* **411**, 167998 (2019).
- [55] P. L. Walters and N. Makri, Quantum–Classical Path

- Integral Simulation of Ferrocene–Ferrocenium Charge Transfer in Liquid Hexane, *J. Phys. Chem. Lett.* **6**, 4959 (2015).
- [56] W. H. Miller, Semiclassical limit of quantum mechanical transition state theory for nonseparable systems, *J. Chem. Phys.* **62**, 1899 (1975).
- [57] W. H. Miller, S. D. Schwartz, and J. W. Tromp, Quantum mechanical rate constants for bimolecular reactions, *J. Chem. Phys.* **79**, 4889 (1983).
- [58] K. Yamashita and W. H. Miller, “Direct” calculation of quantum mechanical rate constants via path integral methods: Application to the reaction path Hamiltonian, with numerical test for the H+H₂ reaction in 3D, *J. Chem. Phys.* **82**, 5475 (1985).
- [59] M. Topaler and N. Makri, Quantum rates for a double well coupled to a dissipative bath: Accurate path integral results and comparison with approximate theories, *J. Chem. Phys.* **101**, 7500 (1994).
- [60] A. Bose and N. Makri, Quantum-classical path integral evaluation of reaction rates with a near-equilibrium flux formulation, *Int. J. Quantum Chem.* , 1 (2021).
- [61] A. Bose and N. Makri, Non-equilibrium reactive flux: A unified framework for slow and fast reaction kinetics, *J. Chem. Phys.* **147**, 152723 (2017).
- [62] A. Ishizaki and G. R. Fleming, Unified treatment of quantum coherent and incoherent hopping dynamics in electronic energy transfer: Reduced hierarchy equation approach, *J. Chem. Phys.* **130**, 234111 (2009).
- [63] M. Rätsep, Z.-L. Cai, J. R. Reimers, and A. Freiberg, Demonstration and interpretation of significant asymmetry in the low-resolution and high-resolution Q y fluorescence and absorption spectra of bacteriochlorophyll a, *J. Chem. Phys.* **134**, 024506 (2011).
- [64] A. Bose and N. Makri, All-Mode Quantum-Classical Path Integral Simulation of Bacteriochlorophyll Dimer Exciton-Vibration Dynamics, *J. Phys. Chem. B* **124**, 5028 (2020).
- [65] S. Kundu and N. Makri, Real-Time Path Integral Simulation of Exciton-Vibration Dynamics in Light-Harvesting Bacteriochlorophyll Aggregates, *J. Phys. Chem. Lett.* **11**, 8783 (2020).
- [66] N. Makri, Modular path integral methodology for real-time quantum dynamics, *J. Chem. Phys.* **149**, 214108 (2018).
- [67] N. Makri, Communication: Modular path integral: Quantum dynamics via sequential necklace linking, *J. Chem. Phys.* **148**, 101101 (2018).
- [68] S. Kundu and N. Makri, Modular path integral for discrete systems with non-diagonal couplings, *J. Chem. Phys.* **151**, 074110 (2019).
- [69] R. Lambert and N. Makri, Memory propagator matrix for long-time dissipative charge transfer dynamics, *Mol. Phys.* **110**, 1967 (2012).
- [70] F. Wang and N. Makri, Quantum-classical path integral with a harmonic treatment of the back-reaction, *J. Chem. Phys.* **150**, 184102 (2019).